



Cite this: *CrystEngComm*, 2021, 23, 3648

Investigation of copper nanoscale electro-crystallization under directed and non-directed electrodeposition from dilute electrolytes†

Mark Aarts,^a Stefan van Vliet,^b Roland Bliem ^b and Esther Alarcon-Llado ^{*a}

Directed electrochemical deposition (DECD) with scanning probes has recently emerged as a bottom-up fabrication alternative to control the 3D morphology at the individual nanostructure level. In order to fabricate functional nanostructures with desired electrical properties, reactivity or stability, it is of utmost importance to control crystal growth. Investigating crystal formation in DECD is not straightforward due to the low fabrication yield and the final structure tending to be an aggregation of multiple particles. Here, we provide a simple method to investigate the early stages of electrochemical growth with atomic force microscopy (AFM). Geometric analysis of AFM topography images provide a rapid and quantitative identification of faceting in nano-crystals, with statistical independence of grain size distribution. We compare the growth evolution in macroscopic electrochemical deposition of Cu on Au with that under directed growth conditions. We find that the directed deposition from micromolar electrolytes in this work is distinctly different than that of conventional copper deposition, but results in similarly shaped spheroidal nuclei as those obtained in macroscopic growth from highly dilute electrolytes. The method presented here opens many possibilities to study *in situ* electrochemical crystal growth or surface stability in operando under electrochemical conditions.

Received 29th January 2021,
Accepted 14th April 2021

DOI: 10.1039/d1ce00143d

rsc.li/crystengcomm

Introduction

Controlling the shape evolution of crystallization processes is an important step in tailoring materials for specific functions.^{1,2} Solution-based growth, such as electrochemical deposition, is a convenient growth method that allows for considerable control over the growth conditions through combinations of solvents, additives, and pH, in addition to heat and pressure.^{3–5} For instance, the evolution of crystal morphology is typically controlled through capping agents that hinder growth from certain crystal facets by specific adsorption.^{6,7} As such, by judiciously choosing growth parameters and environment, morphology related properties can be tuned for a wide variety of applications ranging from catalysis to nano-photonics.^{8–10}

Recently, localised electrochemistry has emerged as a new way to direct the growth in space as it happens, in a 3D printing fashion.^{11–15} Moving scanning probes and pipettes have been shown to direct growth for a number of metals and semiconductors into intricate 3D nanostructures. Most

of these methods can be considered to operate far from equilibrium conditions and the final structures are formed by the agglomeration of small islands/particles. Studying the early stages of electro-crystallization is often not trivial.^{16–19} In fact, even in the well-studied case of electrodeposition of planar metal films, many fundamental questions remain. For instance, recent *in situ* transmission electron microscopy (TEM) and scanning probe microscopy (SPM) measurements have revealed different growth dynamics at the individual nucleus level as compared to classical electro-crystallization models.^{18,20} This is even more complex in the case of directed electrochemical growth, where the low density and small volume of the deposits hampers the use of standard characterisation methods, such as X-ray diffraction, X-ray photoelectron spectroscopy (XPS) or TEM.

In this work, we use *in situ* and *ex situ* atomic force microscopy (AFM) to investigate crystal growth in copper electro-crystallization localized and directed by a moving nanoelectrode in close proximity of a gold substrate in a highly dilute electrolyte, as recently demonstrated by us.¹⁵ Copper and its oxides are particularly important active elements for CO₂ reduction, gas sensors and photocatalysis.²¹ AFM mapping of the growing nanocrystals yields high resolution imaging of their surface, which holds information on crystal orientation through faceting. We combine AFM topography, to obtain the overall size, with

^a Center for Nanophotonics, AMOLF, Science Park 109, Amsterdam, Netherlands.

E-mail: e.alarconllado@amolf.nl

^b Advanced Center for Nanolithography, ARCNL, Science Park 106, Amsterdam, Netherlands

† Electronic supplementary information (ESI) available. See DOI: 10.1039/d1ce00143d

inclination mapping to highlight the shape and orientation of nanoscale growth centres. As such, one can investigate early stages of growth or small metal clusters, where topography alone is not always conclusive in identifying facets and crystal orientations. The crystal growth in directed nanoscale-electrochemistry is compared to that in macro-electrochemical copper deposition. We find that the nanoscale deposits resemble a spheroidal shape similar to those found in macroscopic electrodeposition under the same conditions, but distinct from typical copper growth in more concentrated electrolytes. We show that the footprint of islands in tip-mediated deposition is limited by the tip size, and that the structure has an increasing aspect ratio after coalescence of individual islands, which is critical for the controlled fabrication of out-of-plane structures.

Results and discussion

We confine and direct Cu^{2+} electrochemical deposition on a Au substrate with nanoscale resolution by translating a biased

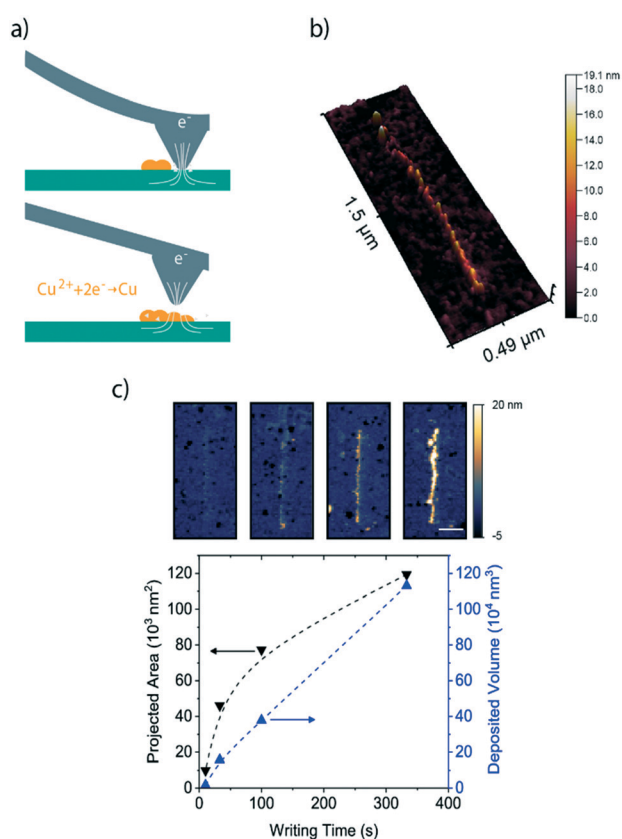


Fig. 1 a) Schematic representation of the direct patterning of electrochemical deposition. b) 3D AFM image of a single Cu line made with directed electrodeposition by translating the AFM tip electrode along a 1 μm long path at 10 nm s⁻¹. c) Projected (footprint) area (black, left) and total deposited volume (blue, right) of directed electrochemical Cu lines for increasing writing time. The latter is varied by means of the translation speed of the tip along the 1 μm long lines. The projected area and volume are obtained from *ex situ* AFM topography maps as shown in the small panels above (scale bar 250 nm).

AFM nano-electrode along a pre-defined path over the substrate's surface, as schematically represented in Fig. 1a. The growth occurs periodically by the local electrostatic interaction of the charged tip with the substrate upon the discharge of the double layer (see ref. 15 for further details on the writing mechanism). To maximise the electrostatic interaction, the salt concentration needs to be low, <10 μM. In this way, we have shown that scanning probe direct writing can deterministically draw structures with a resolution of ~50 nm, as the example of a line shown in Fig. 1b. In this case, the tip was translated at a speed of 10 nm s⁻¹, resulting in a more or less continuous line that appears to consist of many individual islands. By decreasing the translation speed of the tip (*i.e.* increasing the writing time), we observe that the particle density in 1 μm-long lines increases rapidly with time at short writing times and gradually saturates as islands coalesce but do not expand laterally. This effect is represented by the projected area (footprint) of individual lines as a function of writing time (Fig. 1c, black data points, see Experimental). In contrast, the total volume of the lines (Fig. 1c, blue data points), as obtained from *ex situ* AFM topography images (ESI-1†), linearly increases with writing time, or total charge passed through the system. The footprint and volume trend with writing time indicates that the tip size limits the width of the written path and out-of-plane growth is favoured at longer writing times.

From AFM topography images of lines fabricated by directed Cu electrodeposition, where the individual islands can be discerned (see Fig. 2a), we observe spheroidal-like particles with no clear facets as those reported in literature for (non-directed) Cu electrodeposition from CuSO_4 salts.^{22,23} The non-directed deposition is shown as a reference in Fig. 2b, where topography was obtained after the non-directed Cu^{2+} electrochemical deposition on Au using 100 mM CuSO_4 electrolyte upon applying -50 mV to the Au *vs.* a Cu reference electrode wire for 6 seconds. Notice that the salt concentration is similar to what is used in standard Cu electrodeposition, and it is five orders of magnitude higher than in our directed growth experiments and it leads to slightly lower pH values (pH ~4 *vs.* ~6 for the dilute electrolyte). In agreement with literature, growth under high salt concentration results in well-defined faceted nanocrystals. As a fairer comparison, we have also performed non-directed Cu^{2+} electrochemical deposition with the same electrolyte conditions as in the directed case (1 μM), the topography of which is shown in Fig. 2c. For the dilute case, we use a macroscopic Cu wire as counter electrode instead of the tip, as a means to replenish copper ions and avoid depletion in the bath. After 50 minutes of potentiostatic growth at -1 V *vs.* Cu wire quasi reference electrode, the gold substrate was covered by small (<100 nm) elongated nanostructures, where longer growth times resulted in higher particle coverage (see Fig. 2c and ESI-3†). The resulting morphology is very different to the concentrated electrolyte case. Similar thin leaf-like morphologies have been found for the (electro)chemical and

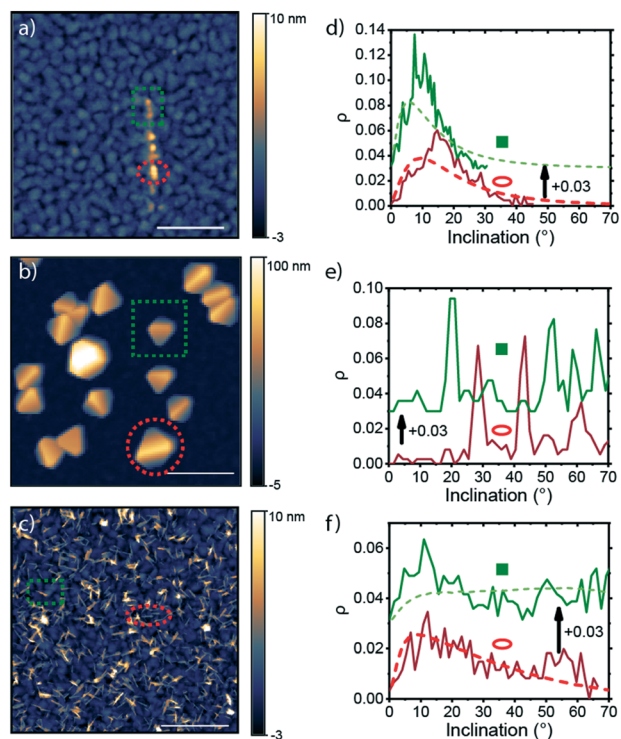


Fig. 2 Left a–c) a) AFM topography of a line written at 10 nm s^{-1} with directed Cu^{2+} electrodeposition, which shows a few individual islands along the writing path. b) AFM topography of non-directed Cu electrodeposition grown from a 100 mM CuSO_4 solution. c) AFM topography of non-directed Cu electrodeposition in the same electrolyte conditions as a) ($1 \mu\text{M CuSO}_4$), showing a random distribution of small fin-like elongated particles. The scale bar in all images is 300 nm . Right d–f) normalised histogram of the angle distributions for the particles indicated on the left. The dashed lines correspond to the expected inclination distribution for a spheroidal shape with dimensions obtained from the topography images. The curves are vertically shifted for clarity.

hydrothermal growth of CuO .^{24,25} Kartal *et al.*²⁴ suggested that CuO or Cu_2O forms during deposition by the spontaneous chemical oxidation of Cu with dissolved oxygen in the electrolyte when the deposition rate is small. Considering the Pourbaix diagram for Cu at room temperature in the absence of an acidic supporting electrolyte, the deposit is expected to consist of Cu for low salt concentration and either Cu or Cu_2O for high salt concentration.^{26,27} Due to the low metal salt concentration yielding a very low current density ($\sim 1 \mu\text{A cm}^{-2}$) and the fact that the solution was exposed to air, the macroscopically grown nanostructures in a dilute electrolyte solution are likely to be oxidized. In fact, we confirm the presence of CuO (90%) and Cu_2O (9%) with XPS characterisation, when growing for 7 hours under these conditions (ESI-3†).

To better assess particle shape and differences between differently grown particles, regardless of overall size, we consider gradient maps, where each pixel represents the magnitude of the local inclination with respect to the substrate through the simple arithmetic operation:²⁸

$$\theta(x,y) = \tan^{-1} \sqrt{(dz/dx)^2 + (dz/dy)^2},$$

where $\theta(x,y)$ is the inclination at the (x,y) position, dx and dy are defined by the scan resolution and dz corresponds to the measured topography. Converted topography images can be found in the ESI† document. Fig. 2d–f show the normalized histogram of the inclination angle within two of the particles in each growth condition, indicated with a colored square or ellipse in Fig. 2a–c. In the angle distribution for the macroscopic growth with a standard solution (Fig. 2e), we observe three to four prominent well-defined peaks in each particle, at $\sim 28^\circ$ and 42° or $\sim 20^\circ$ and 50° , arising from the two facets that can be seen in the particles in Fig. 2b. The $\sim 70^\circ$ angle between the two facets in both particles is in good agreement with that expected between the $\{111\}$ planes of a Cu crystal with respect to a $\{110\}$ base. The broad peaks at around 60° and 67° are likely an artefact due to the tip shape. Despite that the nominal tip shape should allow access to angles up to $65\text{--}75^\circ$, we observe that the main contribution to the high angle peak comes from the edges of the particle, where tip convolution is expected.

In contrast, in both cases where dilute electrolytes were used, the angle distribution is broad, asymmetric, and centred at small angles (Fig. 2d and f), which is well reproduced by that of the top half of a spheroid (dashed curves) with base size and height as given by the topography images (see additional information on the spheroid analysis, and histograms for additional islands in ESI-4†). In the case of directed growth, the particle footprint is more symmetric, and the base-to-height aspect ratio is smaller, giving rise to a narrower angle distribution as compared to that grown in the regular EC-cell. We also observe some deviation in the angle distribution from that of a spheroid. A peak at low angles (around 10° for the particle marked in green and at $\sim 15^\circ$ for that marked in red in Fig. 2a) and the absence of angles from 30° and onwards deviate from the simple spheroid shape. Both deviations can be attributed to a slightly slanted base around the particle that is consistently found in islands in direct-written lines (ESI-4†). In the case of non-directed growth, a broad secondary peak in angle distribution can be discerned around $55\text{--}60^\circ$, which we attribute again to a tip artefact.

To investigate the island growth kinetics and shape evolution of nanoscale directed growth compared to self-assembly we use the analysis developed by Guo *et al.*,²⁹ where geometrical parameters of individual particles of multiple sizes are considered. Comparing the geometric information of particles of different size provides information about growth kinetics, where it is assumed that each island grows independently and obeys the same growth law. Fig. 3a plots the volume and projected area obtained from AFM topography images of islands found in multiple direct-written lines by translating the tip along $1 \mu\text{m}$ long trajectory (red markers). Particles are defined by a pre-defined height threshold in the topography maps (see Experimental section, ESI-3 and ESI-5†). We have considered several different conditions for the directed growth, such as voltage and AFM

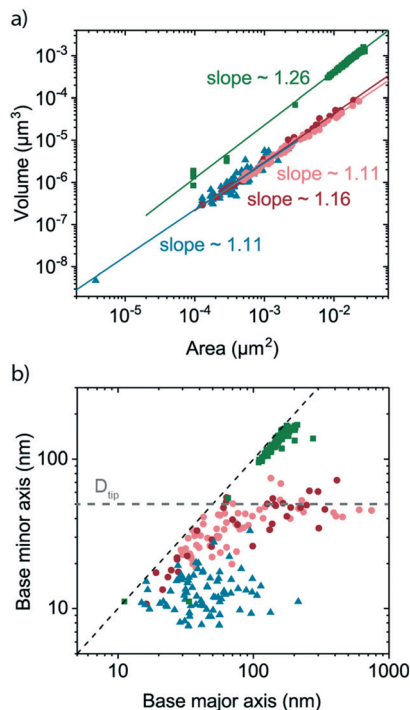


Fig. 3 Particle shape evolution analysis. a) Volume and footprint area plot for multiple individual particles grown under different conditions. Light and dark red circles: directed growth from 1 μM CuSO₄(aq); blue triangles: non-directed growth from 1 μM CuSO₄(aq); green squares: non-directed growth from 100 mM CuSO₄(aq). The geometrical parameters have been obtained by *ex situ* scan-assist AFM topography images, as explained in the Experimental section. The solid line represents the ideal isotropic hemispherical growth case. The dashed lines are power law fits to the data points. b) Footprint (a) symmetry evolution represented by the minor vs. major axis for the equivalent ellipse of multiple individual particles. Different markers correspond to different growth conditions as in a).

writing parameters. Similarly, we also include geometrical data from individual particles obtained from non-directed growth conditions from the dilute electrolyte (blue markers). As reference, we also include the volume and footprint area of copper particles grown from a higher concentration of 100 mM CuSO₄ (green markers). AFM and SEM images of the latter are shown in the ESI-2.†

As explained in ref. 29, the volume (V) and footprint (A) of a growing particle increase following the power-law:

$$V = \alpha A^m$$

where α is a proportionality constant that depends on the particle shape (e.g. $\alpha = 1/2$ or 1 for a spherical or cubic shape, respectively) and m carries information about the growth mechanism. The latter is also the slope in a double-logarithmic representation and is defined as $m = 1 + b/2a$, where a and b are the corresponding exponents for the lateral and vertical growth over time, respectively (i.e. width \propto time ^{a} and height \propto time ^{b}). Consequently, the m -slope reveals whether the particle grows isotropically ($a = b$ and thus $m = 1.5$), preferentially in-plane ($a > b$, $m < 1.5$) or preferentially

out-of-plane ($a < b$, $m > 1.5$). It is interesting to note that for the dilute electrolyte, geometrical data of all particles follow a common trend with a slope of $m \sim 1.1$ as obtained from fitting a power-law to the data regardless of growth conditions (directed or non-directed). This analysis confirms preferential in-plane growth for the dilute electrolyte. This is in contrast to particle growth in more standard electrochemical conditions (100 mM CuSO₄), which is represented by the green data points. In agreement with literature,³⁰ we find that the growth in standard electrochemical conditions to be more isotropic with a slope of $m \sim 1.26$ in the double-logarithmic representation.

The similar slopes found in the two growth methods from the dilute electrolyte initially suggests that confining electro-deposition does not influence the growth kinetic mechanism, but it is ruled by the electrolyte. However, despite the area-volume relation being the same, we find that the non-directed grown nanostructures are generally more elongated and wire-like (see also Fig. 2). To better illustrate the progression of the nanostructure footprint, Fig. 3b represents the largest and smallest in-plane dimensions (major and minor axis from a fitted ellipse, respectively) of the same individual particles as in Fig. 3a. As expected from the AFM and SEM images, self-assembled nanostructures (blue data points) preferentially grow along one of the two in-plane dimensions (i.e. highly anisotropic), which leads to thin elongated structures where the thickness is observed to be limited to <10 nm for single rods, only growing higher at much longer growth times, where individual rods also start to overlap (ESI-3†). As mentioned earlier, the slow deposition rate could lead to copper oxidation, which self-limits the crystal thickness and results into highly anisotropic CuO growth. In these conditions, the deposition rate is limited by the low ion concentration.

On the other hand, in directed deposition (red data points) the in-plane growth is notably isotropic until the particle size reaches the tip diameter (~ 50 nm, indicated by the grey dashed line), at which point the particle width (in the direction perpendicular to the writing direction) saturates. It should be noted that the data points for the largest major axes consider a more or less fully coalesced line (1 μm). The particle evolution in directed deposition resembles that found in the electrochemical copper deposition from 100 mM CuSO₄ in this aspect (green data points). In this case, the in-plane growth is clearly isotropic as the two in-plane dimensions are approximately the same as the particles grow (Fig. 3b). We believe that despite the low ion concentration, the close proximity of the tip counter electrode to the substrate facilitates a faster deposition rate compared to the non-directed case with the same electrolyte conditions, evidenced by the fact that a much longer deposition time was required to grow the non-directed sample compared to the lines (factor 30 for the images in Fig. 2), despite yielding smaller islands. On the other hand, the fact that the vertical growth is hampered in the directed case as compared to growth from a non-dilute electrolyte, we

believe is likely due to the restricted ion access by the tip itself. A 2D radial diffusion of ions towards the deposit would promote an increasing lateral growth rate ($a > 1$, and $m < 1.5$) and thus decrease the aspect ratio over time.

Conclusions

In this paper we use the geometrical data obtained with AFM to investigate the electrochemical growth of nanoscale copper particles from a highly dilute (1 μM) electrolyte. We distinguish and compare growth in a regular 3-electrode electrochemical cell and growth directed by a nanoelectrode AFM tip. From the topography images we show that the growth of copper can be directed out-of-plane using tip-mediated growth, if the tip speed is low enough for different islands to coalesce. We analyse the shape of these copper islands through the inclination distribution, which shows that they have a spheroidal shape in both dilute cases, in contrast to copper growth at higher concentrations. Furthermore, we show that the early stage of growth in the dilute electrolyte is preferentially in-plane for both the directed and non-directed deposition. A striking difference however is that lateral growth is confined to 1 dimension in the non-directed deposition, similar to shapes observed in copper oxide species; whereas the tip-mediated growth is isotropic in-plane, until it reaches the bounds of the tip diameter. The latter is comparable to the growth in more concentrated electrolytes.

Experimental

Sample fabrication and electrodeposition

For the direct writing, we use a 2-electrode configuration consisting of an insulated AFM tip, except for a Pt coated apex,³¹ and the metal substrate. The potential is controlled by either a CH760E or a BioLogic SP-300 potentiostat. The substrate electrode consists of a silicon substrate coated with a chromium adhesion layer and a gold top layer contacted from the top. Electrodeposition was done from 100 mM and 1 μM aqueous (MilliQ®, 18.2 $\text{M}\Omega\text{ cm}$) copper sulfate solutions ($\text{CuSO}_4 \cdot 5\text{H}_2\text{O}$, 99.995% from Sigma-Aldrich). The low concentration electrolyte was prepared before every experiment from a 1 mM $\text{CuSO}_4(\text{aq})$ stockpile and diluted (1000 \times) using fresh MilliQ water. Due to the hydrolysis of CuSO_4 , the solution is more acidic for the higher salt concentration (pH ~ 4 vs. 6). The electrochemical cell used for the *in situ* mapping of copper nuclei, and the nanoscale deposition is shown schematically in ESI-6.† The nondirected deposition from the dilute electrolyte was done in an electrochemical cell outside of the AFM setup, with an exposed electrode area of 1.5 cm^2 using a coiled copper wire as the counter electrode. The measured open circuit potential in this cell for the 1 μM CuSO_4 electrolyte is $\sim 650 \pm 90$ mV vs. Cu QRE (obtained for 7 samples, as shown in ESI-7†).

Atomic force microscopy (AFM)

AFM measurements were performed using a Bruker Dimension Icon. The protocol for the directed nanoscale

writing is explained in depth in ref. 15. The *in situ* images as shown in Fig. 2b, and ESI-2† are obtained with the ScanAsyst-Fluid+ probe (Bruker, nominal tip radius 2 nm), in PeakForce tapping mode. *Ex situ* images were obtained with the ScanAsyst-Air probe (Bruker, nominal tip radius 2 nm). *Ex situ* images were also used for the directed nanoscale deposition as the SECM probe used for the deposition was relatively large compared to the features of interest (nominal radius 25 nm).

AFM data treatment

AFM images were treated by removing the polynomial background (first or second order) and removing image defects by aligning rows or removing scars using the Gwyddion software.³² The shape analysis is done using height thresholding and considering the pixels underneath the resulting mask. Projected (footprint) area and deposited volume (Fig. 1) are obtained using a height threshold of 2 nm ($\sim 3\times$ the sample roughness) for every written line. The masks in Fig. 2 are obtained by manually identifying the islands and combining that with a height threshold, the histogram was then obtained using the slope distribution tool, with inclination maps constructed through the arithmetic operation as mentioned in the main text (ESI-4†). Similarly, for the data in Fig. 3, the area of interest was combined with height thresholding after which the grain correlation tool was used to get projected area vs. volume and major vs. minor axis of the equivalent ellipse (the numbers in Fig. 3 are multiplied by 2 to reflect diameters rather than radii).

XPS measurements

XPS spectra were acquired using a Scienta Omicron HiPP-3 analyzer using an entrance slit of 2.5 mm, and a monochromatic Al $\text{K}\alpha$ source operating at 20 mA emission current. The base pressure was $\sim 2 \times 10^{-9}$ mbar, and the operating pressure was $\sim 5 \times 10^{-9}$ mbar. Survey and high-resolution spectra were acquired at pass energies of 500 eV and 100 eV respectively. Data analysis and quantification were performed using KolXPD from KolibriK.

Author contributions

MA and EAL designed the experiments. MA conducted the electrodeposition and atomic force microscopy measurements. These measurements were analysed by MA and EAL. SvV conducted the XPS measurements. XPS measurements were analysed by SvV and RB. MA and EAL drafted the manuscript. All authors reviewed and commented on the manuscript.

Conflicts of interest

There are no conflicts to declare.

Acknowledgements

This work is part of the research program at the Netherlands Organisation for Scientific Research (NWO). Part of this work has been carried out at the Advanced Research Center for Nanolithography (ARCNL), a public-private partnership of the University of Amsterdam (UvA), the Vrije Universiteit Amsterdam (VU), the Netherlands Organisation for Scientific Research (NWO), and the semiconductor equipment manufacturer ASML. Authors thank D. Ursem and the design and precision manufacturing departments at Amolf for their support. We also thank Dr. M. Valenti and Prof. E. Garnett for fruitful discussions.

References

- 1 B. Roldan Cuenya, Metal Nanoparticle Catalysts Beginning to Shape-up, *Acc. Chem. Res.*, 2013, **46**, 1682–1691.
- 2 N. Tian, Z. Zhou and S. Sun, Platinum Metal Catalysts of High-Index Surfaces: From Single-Crystal Planes to Electrochemically Shape-Controlled Nanoparticles, *J. Phys. Chem. C*, 2008, **112**, 19801–19817.
- 3 L. Guo and P. C. Searson, Anisotropic Island Growth: A New Approach to Thin Film Electrocrystallization, *Langmuir*, 2008, **24**, 10557–10559.
- 4 L. Huang, *et al.* Shape regulation of high-index facet nanoparticles by dealloying, *Science*, 2019, **365**, 1159–1163.
- 5 M. L. Personick, M. R. Langille, J. Zhang and C. A. Mirkin, Shape control of gold nanoparticles by silver underpotential deposition, *Nano Lett.*, 2011, **11**, 3394–3398.
- 6 M. J. Siegfried and K.-S. Choi, Directing the Architecture of Cuprous Oxide Crystals during Electrochemical Growth, *Angew. Chem.*, 2005, **117**, 3282–3287.
- 7 H.-G. Liao, *et al.* Facet development during platinum nanocube growth, *Science*, 2014, **345**, 916–919.
- 8 H. Robotjazi, *et al.*, Plasmon-induced selective carbon dioxide conversion on earth-abundant aluminum-cuprous oxide antenna-reactor nanoparticles, *Nat. Commun.*, 2017, **8**, 27.
- 9 N. Tian, Z.-Y. Zhou, S.-G. Sun, Y. Ding and Z. L. Wang, Synthesis of Tetrahedral Platinum Nanocrystals with High-Index Facets and High Electro-Oxidation Activity, *Science*, 2007, **316**, 732–735.
- 10 R. Jin, *et al.* Photoinduced Conversion of Silver Nanospheres to Nanoprisms, *Science*, 2001, **294**, 1901–1903.
- 11 D. M. Kolb and F. C. Simeone, Nanostructure formation at the solid / liquid interface, *Curr. Opin. Solid State Mater. Sci.*, 2006, **9**, 91–97.
- 12 S. Daryadel, *et al.*, Localized Pulsed Electrodeposition Process for Three-Dimensional Printing of Nanotwinned Metallic Nanostructures, *Nano Lett.*, 2018, **18**, 208–214.
- 13 L. Hirt, A. Reiser, R. Spolenak and T. Zambelli, Additive Manufacturing of Metal Structures at the Micrometer Scale, *Adv. Mater.*, 2017, **29**, 1604211.
- 14 A. Reiser, M. Lindén and P. Rohner, *et al.*, Multi-metal electrohydrodynamic redox 3D printing at the submicron scale, *Nat. Commun.*, 2019, **10**, 1853.
- 15 M. Aarts and E. Alarcon-Llado, Directed nanoscale metal deposition by the local perturbation of charge screening at the solid-liquid interface, *Nanoscale*, 2019, **11**, 18619–18627.
- 16 G. Staikov, Nanoscale electrodeposition of low-dimensional metal phases and clusters, *Nanoscale*, 2016, **8**, 13880–13892.
- 17 S. C. S. Lai, R. A. Lazenby, P. M. Kirkman and P. R. Unwin, Nucleation, aggregative growth and detachment of metal nanoparticles during electrodeposition at electrode surfaces, *Chem. Sci.*, 2015, **6**, 1126–1138.
- 18 R. L. Harniman, *et al.*, Real-time tracking of metal nucleation via local perturbation of hydration layers, *Nat. Commun.*, 2017, **8**, 971.
- 19 H. E. M. Hussein, *et al.*, Tracking Metal Electrodeposition Dynamics from Nucleation and Growth of a Single Atom to a Crystalline Nanoparticle, *ACS Nano*, 2018, **12**, 7388–7396.
- 20 M. J. Williamson, R. M. Tromp, P. M. Vereecken, R. Hull and F. M. Ross, Dynamic microscopy of nanoscale cluster growth at the solid-liquid interface, *Nat. Mater.*, 2003, **2**, 532–536.
- 21 S. Nitopi, *et al.*, Progress and Perspectives of Electrochemical CO₂ Reduction on Copper in Aqueous Electrolyte, *Chem. Rev.*, 2019, **119**, 7610–7672.
- 22 D. Grujicic and B. Pesic, Electrodeposition of copper: the nucleation mechanisms, *Electrochim. Acta*, 2002, **47**, 2901–2912.
- 23 P. Grosse, *et al.* Dynamic Changes in the Structure, Chemical State and Catalytic Selectivity of Cu Nanocubes during CO₂ Electroreduction: Size and Support Effects, *Angew. Chem., Int. Ed.*, 2018, **57**, 6192–6197.
- 24 C. Kartal, Y. Hanedar, T. Öznülüer and Ü. S. Demir, Morphology, and Size-Controlled Electrochemical Fabrication of Cu x O (x = 1, 2) at Underpotential, *Langmuir*, 2017, **33**, 3960–3967.
- 25 L. Zhang, *et al.*, Cu₂O–CuO composite microframes with well-designed micro/nano structures fabricated via controllable etching of Cu₂O microcubes for CO gas sensors, *CrystEngComm*, 2013, **15**, 7462.
- 26 B. Beverskog and I. Puigdomenech, Revised Pourbaix Diagrams for Copper at 25 to 300°C, *J. Electrochem. Soc.*, 1997, **144**, 3476–3483.
- 27 M. J. Siegfried and K.-S. Choi, Electrochemical Crystallization of Cuprous Oxide with Systematic Shape Evolution, *Adv. Mater.*, 2004, **16**, 1743–1746.
- 28 F. B. Basset, *et al.*, High-Yield Fabrication of Entangled Photon Emitters for Hybrid Quantum Networking Using High-Temperature Droplet Epitaxy, *Nano Lett.*, 2018, **18**, 505–512.
- 29 L. Guo, G. Oskam, A. Radisic, P. M. Hoffmann and P. C. Searson, Island growth in electrodeposition, *J. Phys. D: Appl. Phys.*, 2011, **44**, 443001.
- 30 L. Guo and P. C. Searson, Influence of anion on the kinetics of copper island growth, *Nanoscale*, 2010, **2**, 2431.
- 31 Z. Huang, *et al.*, PeakForce Scanning Electrochemical Microscopy with Nanoelectrode Probes, *Microsc. Today*, 2016, **24**, 18–25.
- 32 D. Nečas and P. Klapetek, Gwyddion: an open-source software for SPM data analysis, *Cent. Eur. J. Phys.*, 2012, **10**, 181–188.